nature chemistry

SUPPLEMENTARY INFORMATION

DOI: 10.1038/NCHEM.1069

Design Principles for Oxygen Reduction Activity on Perovskite Oxide Catalysts for Fuel Cells and Metal-Air Batteries

Jin Suntivich[1,†], Hubert A. Gasteiger[2,†,§], Naoaki Yabuuchi[2,†],
Haruyuki Nakanishi[3], John B. Goodenough[4], Yang Shao-Horn*[,1,2,†]

[1] *Materials Science and Engineering Department,*
[2] *Mechanical Engineering Department,*
[†] *Electrochemical Energy Laboratory,*
Massachusetts Institute of Technology, 31-056,
77 Massachusetts Ave, Cambridge, MA 02139, USA

[3] *Fuel Cell System Development Division, Toyota Motor Corporation*
Higashifuji Technical Center 1200, Mishuku, Susono, Shizuoka 410-1193, Japan

[4] *Texas Materials Institute, University of Texas at Austin,*
ETC 9.184, Austin, TX 78712, USA

[§] *Present Address: Department of Chemistry, Technische Universität München,*
Lichtenbergstrasse 4, D-85747 Garching, Germany

* E-mail: shaohorn@mit.edu

Supplementary methods

Soft X-ray Absorption characterization. O K-edge XAS was collected at Saga Synchrotron (BL12), Japan. All measurements were collected in electron-yield mode at 10^{-7} Pa pressure. All spectra were normalized to the O atomic absorption at ~550 eV. In a band corresponding to the O *1s* to B *3d* - O *2p* excitation, the spectra probe the *u* symmetry portion of the unoccupied state, but not the *g* symmetry portion as the latter is forbidden by the selection rule. In a pseudocubic approximation of the perovskite structure, the *u* symmetry portion is intrinsic to the 2p orbital of the O atom and the absorbance is related to the unoccupied 2p orbital ("ligand hole"). The amount of the hybridization is defined by the intensity of the ligand-hole normalized to the density of the B *3d* - O *2p* unoccupied state, viz., the ligand character of each B *3d* – O *2p* hole. To account for the difference in the ligand-hole strength between the e_g symmetry and the t_{2g} symmetry, an appropriate prefactor assuming 2x reduction in t_{2g} transfer integral in comparison to e_g (which corresponds to 4x reduction in ligand-hole strength) is applied[1]. Applying the dipole operator approximation, the hybridization of B and O atoms in an octahedral environment can be quantified by the following parameter:

$$|\beta|^2 \propto \frac{\text{Absorbance}}{\text{hole}_{E_g} + \frac{1}{4}\text{hole}_{T_{2g}}}$$

In this definition, absorbance is the integrated area of the O *1s* → B *3d* - O *2p* band in the O K-edge minus the fitted linear background (see Figure 4a)[2], and the holes (unoccupied states) for e_g and t_{2g} are defined by the unoccupied density of states of e_g and t_{2g} orbitals respectively (see Table S1 for values). The ¼ prefactor of the t_{2g} hole accounts for the difference in transfer integral between t_{2g} and e_g.

Hard X-ray Absorption characterization. *Hard* XAS was collected at beamline X11A of the National Synchrotron Light Source at the Brookhaven National Laboratory with the electron storage ring of 2.8 GeV and a current in the range of 150-300 mA. The Mn, Ni, Co, and Fe K-edge electron yield modes were collected from oxide powders mounted on carbon conductive tape with a Lytle detector at room temperature using Si(111) double-crystal monochromator detuned to ~70% of the maximum intensity. The spectra were calibrated to the reference metal foils by setting the maximum inflection points (E_0) to their respective reference energies. X-ray absorption near edge structure (XANES) was extracted from the absorbance with the IFEFFIT package by subtracting from the pre-edge region with a linear fit and normalizing to a per atomic basis with the average of the absorption cross section over the post-edge region[3].

Determination of e_g filling of non-stoichiometric $LaMnO_{3+\delta}$. Based on the published thermodynamics, subjecting $LaMnO_3$ to a heat treatment in air at 800°C will result in a phase transformation to an oxygen over-stoichiometric $LaMnO_{3+\delta}$ compound with $\delta \approx 0.11$ (± 0.05)[4]. To ensure that the synthesis of $LaMnO_{3+\delta}$ was successful, XRD was collected to confirm the rhombohedral phase of $LaMnO_{3+\delta}$ (Table S2). From the published $\delta \approx 0.11$, $LaMnO_{3+\delta}$ has a high spin $t_{2g}^3 e_g^{0.79}$ configuration and e_g filling of 0.79 (± 0.05) ≈ 0.8[4].

Determination of e_g filling of Ca-substituted $La_{0.5}Ca_{0.5}MnO_3$. Previous studies using X-ray emission spectroscopy[4], thermogravimetric analysis (TGA)[6], X-ray absorption near-edge spectroscopy (XANES)[5], and magnetic measurement[6] have shown that charge compensation following Ca-substitution in $LaMnO_3$ occurs via Mn^{4+} formation. We, therefore, assume that our $La_{0.5}Ca_{0.5}MnO_3$ compound charge-compensates by forming

Mn^{4+}. As a result, $La_{0.5}Ca_{0.5}MnO_3$ has an average Mn oxidation state of 3.5+ and therefore an electron configuration of $t_{2g}^{3} e_g^{0.5}$. We had conducted Mn K-edge XANES to confirm that the Mn in $La_{0.5}Ca_{0.5}MnO_3$ shifts to higher oxidation state in relative to $LaMnO_3$ (Figure S3a).

Determination of e_g filling of Ca-substituted $La_{0.75}Ca_{0.25}FeO_3$ and $La_{0.5}Ca_{0.5}FeO_3$. The charge compensation following Ca-substitution in $LaFeO_3$ is assumed to occur via Fe^{4+} formation in high spin configuration. This is in agreement with the observation of Fe^{4+} formation in Ca-substituted $LaFeO_3$ using Mossbäuer spectroscopy[9,10]. Our own Fe K-edge XANES also confirms that the Fe oxidation shifts to higher oxidation state with increasing Ca content (Figure S3b).

Determination of e_g filling of Ca-substituted $La_{0.5}Ca_{0.5}CoO_{3-\delta}$. Because the exact spin-state of $La_{0.5}Ca_{0.5}CoO_{3-\delta}$ has not been determined yet in the literature, partly due to the fact that the majority of Co remains 3+ despite the substitution of La^{3+} by Ca^{2+} ion[11], we approximate the spin state of this compound as a mixture of $LaCoO_3$ and $SrCoO_{2.5}$. Using a mixture of intermediate spin $LaCoO_3$ $(t_{2g}^{5} e_g^{1})^7$ and high spin $SrCoO_{2.5}$ $(t_{2g}^{4} e_g^{2})^8$, we arrive at an approximation of $e_g \approx 1.5$ for $La_{0.5}Ca_{0.5}CoO_{3-\delta}$. The concept of high-spin Co stabilization with Ca-substitution has been proposed in the literature[11,14], so we believe our approximation is within reason, especially for the surface Co. We had also conducted TGA to confirm the formation of oxygen vacancy ($\delta_{TGA} = 0.21 \pm 0.01$) that had been reported in the literature following Ca-substitution. Our Co K-edge XANES additionally demonstrated that the Co edge remained unchanged following Ca-substitution, which provides further evidence for the stabilization of Co^{3+} in $La_{0.5}Ca_{0.5}CoO_{3-\delta}$ (Figure S3c).

Determination of e_g filling of $LaNi_{0.5}Mn_{0.5}O_3$ and $LaCu_{0.5}Mn_{0.5}O_3$. The e_g filling for the mixed B-site compounds ($LaNi_{0.5}Mn_{0.5}O_3$ and $LaCu_{0.5}Mn_{0.5}O_3$) is complicated by the presence of two inequivalent B atoms and thus two different e_g fillings. In addition, it is widely known that a charge-ordered Mn/Ni undergoes charge-disproportionation into Mn^{4+} and Ni^{2+} in $LaNi_xMn_{1-x}O_3$[15]. Thus, to determine properly the e_g filling for the mixed compounds, the oxidation state of both B atoms was measured with XANES. Using a known-relationship where E_0 (maximum inflection point of the absorption edge) scales with oxidation state[9], we estimate the valence state of Mn in both $LaNi_{0.5}Mn_{0.5}O_3$ and $LaCu_{0.5}Mn_{0.5}O_3$ to be 3.7 (high spin configuration, Figure S4a). A high-spin configuration of Mn leads to an e_g filling of 0.3 for the Mn site. Similar analysis was applied to Ni in $LaNi_{0.5}Mn_{0.5}O_3$, and the oxidation state of 2.3 was found (Figure S4b.) Based on this information, the e_g filling for Ni is thus determined to be 1.7 (low-spin configuration). While we did not perform this analysis on Cu in $LaCu_{0.5}Mn_{0.5}O_3$, we believe the Cu oxidation state should be close to that of Ni if not lower due to the higher electronegativity of Cu atom. Furthermore, the similarity in the Mn oxidation state between $LaNi_{0.5}Mn_{0.5}O_3$ and $LaCu_{0.5}Mn_{0.5}O_3$ also indicates that the Cu and the Ni oxidation state should be very close to each other (≈2.3+). Thereby, we conclude that the e_g filling for Cu is 2.7 or higher. When we apply the e_g filling from either Mn or Ni (Cu) to the volcano plot, we have found that the use of e_g filling from Mn is most consistent with the observed activity trend (Figure 2a). Had we used the e_g filling of average B atoms, or Ni or Cu, the e_g would have resulted in an underestimation of the ORR activity. The consistency of selecting Mn e_g filling with our volcano plot also leads us to propose that the active site on the mixed compounds is the Mn atom, where both Ni and Cu atoms

had too many e_g electrons, rendering their catalytic properties inactive. The proposed Mn active site is consistent with our observation with the Ruddlesden-Popper compounds that Ni(+2) and Ni(+2.5) were not active for the ORR. Hence it is unlikely that Ni(2.3+), which was observed in $LaNi_{0.5}Mn_{0.5}O_{3,}$ would be the active site.

Table S1. Summary of literature information on the spin state of the perovskite oxides

	Valence	Spin state	Assignment	Example of reference
$LaCrO_3$	Cr^{3+}	n/a	t_{2g}^3	LS and HS identical
$LaMnO_3$	Mn^{3+}	H.S.	$t_{2g}^3 e_g^1$	Magnetization[6]
$LaFeO_3$	Fe^{3+}	H.S.	$t_{2g}^3 e_g^2$	Mossbäuer spectroscopy[10]
$LaCoO_3$	Co^{3+}	I.S.	$t_{2g}^5 e_g^1$	Magnetization[11]
$LaNiO_3$	Ni^{3+}	L.S.	$t_{2g}^6 e_g^1$	Extrapolation from $RNiO_3$ magnetization[12,13]
La_2NiO_4	Ni^{2+}	n/a	$t_{2g}^6 e_g^2$	LS and HS identical
$La_4Ni_3O_{10}$	$Ni^{2.7+}$	L.S.	$t_{2g}^6 e_g^{1.3}$	Extrapolation from $LaNiO_3$ and La_2NiO_4
$LaNi_{0.5}Mn_{0.5}O_3$	$Mn^{3.7+}$ $Ni^{2.3+}$	H.S. (Mn) L.S. (Ni)	$t_{2g}^3 e_g^{0.3}$ (Mn) $t_{2g}^6 e_g^{1.7}$ (Ni)	See Supplementary Method
$LaCu_{0.5}Mn_{0.5}O_3$	$Mn^{3.7+}$ $Cu^{2.3+}$	H.S. (Mn) L.S. (Cu)	$t_{2g}^3 e_g^{0.3}$ (Mn) $t_{2g}^6 e_g^{2.7}$ (Cu)	See Supplementary Method
$La_{0.5}Ca_{0.5}CrO_{3-\delta}$ (Assume $\delta = 0$)	$Cr^{2.5+}$	n/a	$t_{2g}^{2.5}$	LS and HS identical
$La_{0.5}Ca_{0.5}MnO_{3-\delta}$ (Assume $\delta = 0$)	$Mn^{3.5+}$	H.S.	$t_{2g}^3 e_g^{0.5}$	Magnetization[6], X-ray Emission[4]
$La_{0.5}Ca_{0.5}FeO_{3-\delta}$ (Assume $\delta = 0$)	$Fe^{3.5+}$	H.S.	$t_{2g}^3 e_g^{1.5}$	Mossbäuer spectroscopy[9,10]
$La_{0.75}Ca_{0.25}FeO_{3-\delta}$ (Assume $\delta = 0$)	$Fe^{3.25+}$	H.S.	$t_{2g}^3 e_g^{1.75}$	Mossbäuer spectroscopy[9,10]
$La_{0.5}Ca_{0.5}CoO_{3-\delta}$ ($\delta_{TGA} = 0.21\pm0.01$)	Co^{3+}	I.S./H.S.	$t_{2g}^{4.5} e_g^{1.5}$	$La_{1-x}Ca_xCoO_{3-\delta}$ extrapolation[11]
$LaMnO_{3+\delta}$ (Assume $\delta = 0.1$)	$Mn^{3.2+}$	H.S.	$t_{2g}^3 e_g^{0.8}$	X-ray Emission Spectroscopy[4]

Table S2. The derived lattice parameters of the oxide model compounds in this work

	Space group	a(Å)	b(Å)	c(Å)
$LaCrO_3$	P n m a	5.48	7.76	5.51
$LaMnO_3$	P n m a	5.66	7.72	5.53
$LaFeO_3$	P n m a	5.57	7.85	5.56
$LaCoO_3$	R -3 c	5.44	5.44	13.09
$LaNiO_3$	R -3 c	5.46	5.46	13.14
La_2NiO_4	F m m m	5.47	5.46	12.68
$La_4Ni_3O_{10}$	F m m m	5.41	5.46	27.99
$LaNi_{0.5}Mn_{0.5}O_3$	P n m a	5.46	7.74	5.51
$LaCu_{0.5}Mn_{0.5}O_3$	P n m a	5.48	7.77	5.52
$La_{0.5}Ca_{0.5}CrO_{3-\delta}$	P n m a	5.42	7.68	5.45
$La_{0.5}Ca_{0.5}MnO_{3-\delta}$	P n m a	5.42	7.65	5.43
$La_{0.5}Ca_{0.5}FeO_{3-\delta}$	P n m a	5.55	7.84	5.55
$La_{0.75}Ca_{0.25}FeO_{3-\delta}$	P n m a	5.52	7.80	5.52
$La_{0.5}Ca_{0.5}CoO_{3-\delta}$	P n m a	5.41	7.59	5.36
$LaMnO_{3+\delta}$	R -3 c	5.52	5.52	13.35

Table S3. Characterizations of the oxides studied in this work.

The number averaged diameter, d_{number}, the volume-area averaged diameter, $d_{v/a}$, and the specific surface area, A_s. were obtained from particle size distribution measurements. Methodology for calculating each variable is given elsewhere[14].

	d_{number} (μm)	$d_{v/a}$ (μm)	A_s ($m^2\ g^{-1}$)
$LaCrO_3$	0.64 (±0.25)	0.83	1.1
$LaMnO_3$	1.05 (±0.52)	1.51	0.6
$LaFeO_3$	0.71 (±0.34)	1.01	0.9
$LaCoO_3$	0.78 (±0.40)	1.10	0.7
$LaNiO_3$	0.20 (±0.06)	0.24	3.5
La_2NiO_4	0.49 (±0.25)	0.70	1.2
$La_4Ni_3O_{10}$	0.45 (±0.15)	0.53	1.6
$LaNi_{0.5}Mn_{0.5}O_3$	0.34 (±0.11)	0.81	1.1
$LaCu_{0.5}Mn_{0.5}O_3$	0.58 (±0.28)	0.80	1.1
$La_{0.5}Ca_{0.5}CrO_{3-\delta}$	0.19 (±0.06)	0.22	4.9
$La_{0.5}Ca_{0.5}MnO_{3-\delta}$	0.92 (±0.44)	0.62	2.1
$La_{0.5}Ca_{0.5}FeO_{3-\delta}$	0.62 (±0.31)	0.89	1.1
$La_{0.75}Ca_{0.25}FeO_{3-\delta}$	0.36 (±0.22)	0.59	1.8
$La_{0.5}Ca_{0.5}CoO_{3-\delta}$	0.43 (±0.23)	0.63	1.6
$LaMnO_{3+\delta}$	1.39 (±0.58)	1.81	0.5

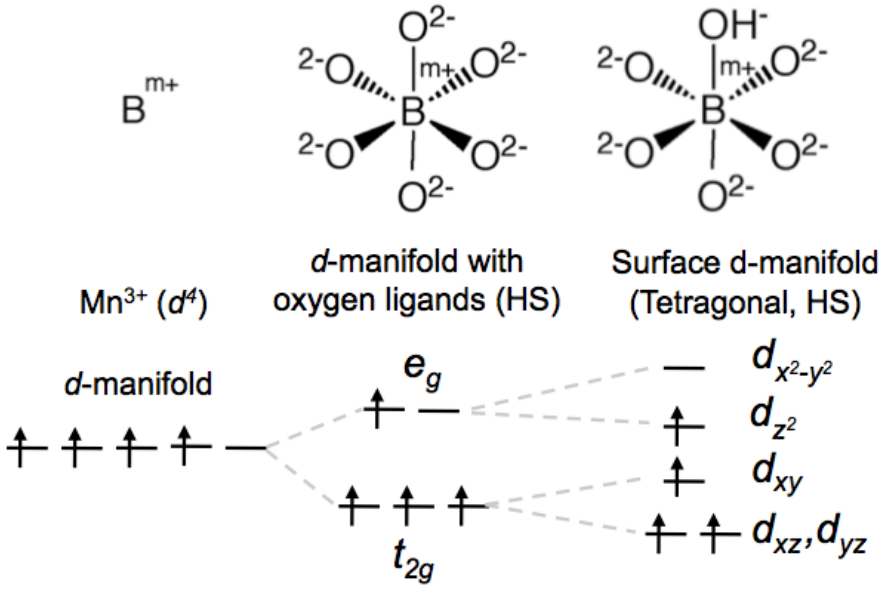

Scheme S1. Molecular orbital of BO_6 interaction. The energy levels of the d-electrons in free B ion, octahedral BO_6, and surface BO_6 configurations. The initial d manifold degeneracy is split into the antibonding e_g and t_{2g} levels. Mn^{3+} (d^4) in high spin configuration is shown as an example of a cation with an antibonding e_g-orbital degeneracy with a single e_g electron. At a surface cation, the degeneracy is removed by a tetragonal site symmetry in which the occupied e_g electron occupying a z^2 orbital directed toward a surface OH^- is lowered in energy relatively to the e_g electron occupying the x^2-y^2 orbital.

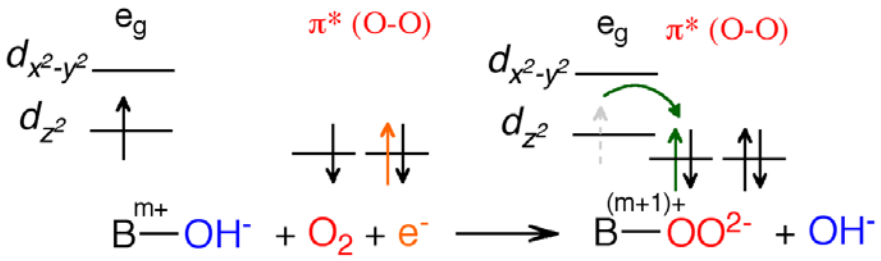

Scheme S2. The transfer of e_g electron during O_2^{2-}/OH^- displacement drives the reaction forward. The rate-limiting step of the ORR is the surface hydroxide displacement. The kinetics of this step is determined by the driving force from the transfer of a σ* electron to an O-O orbital.

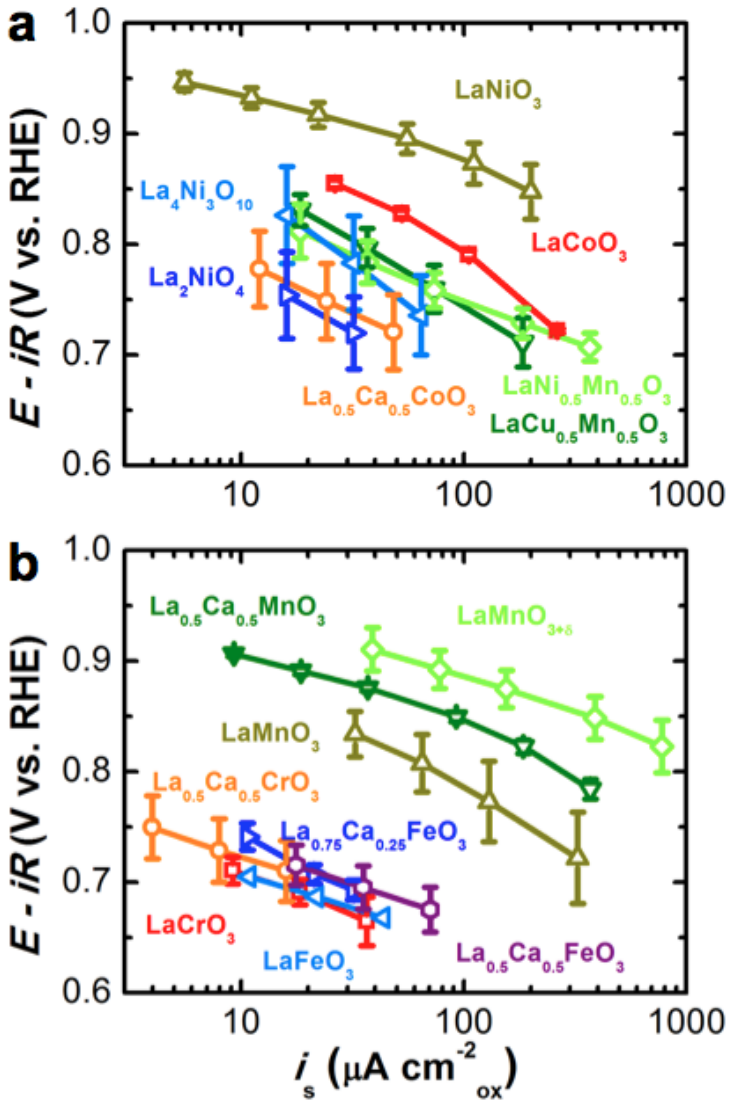

Figure S1. (A-B) Tafel plot of the ORR specific activity of various oxides studied in this work using thin film RDE. All the activities are transport-compensated, iR-corrected, and normalized to the catalyst surface area.

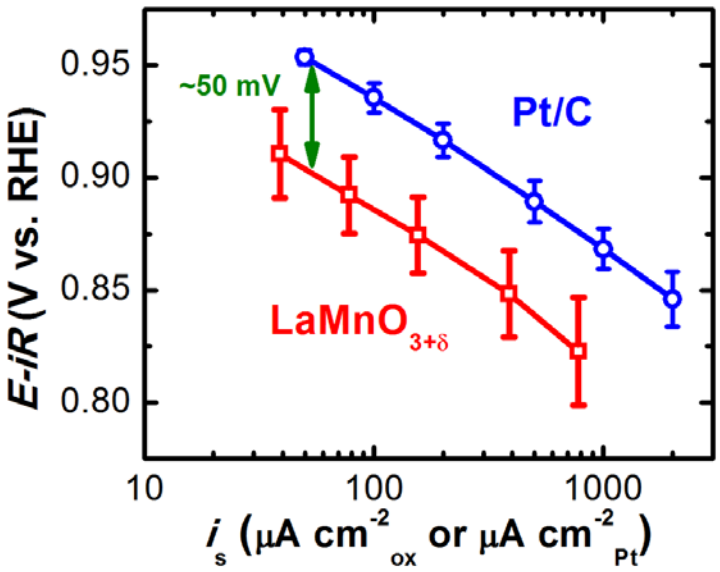

Figure S2. Tafel plot of the ORR specific activity of $LaMnO_{3+\delta}$ vs. Pt/C from the thin film RDE experiments. These two catalysts have very similar ORR activities (~50 mV shift, corresponding to less than an order of activity difference). Error bars represent standard deviations of at least three independent measurements.

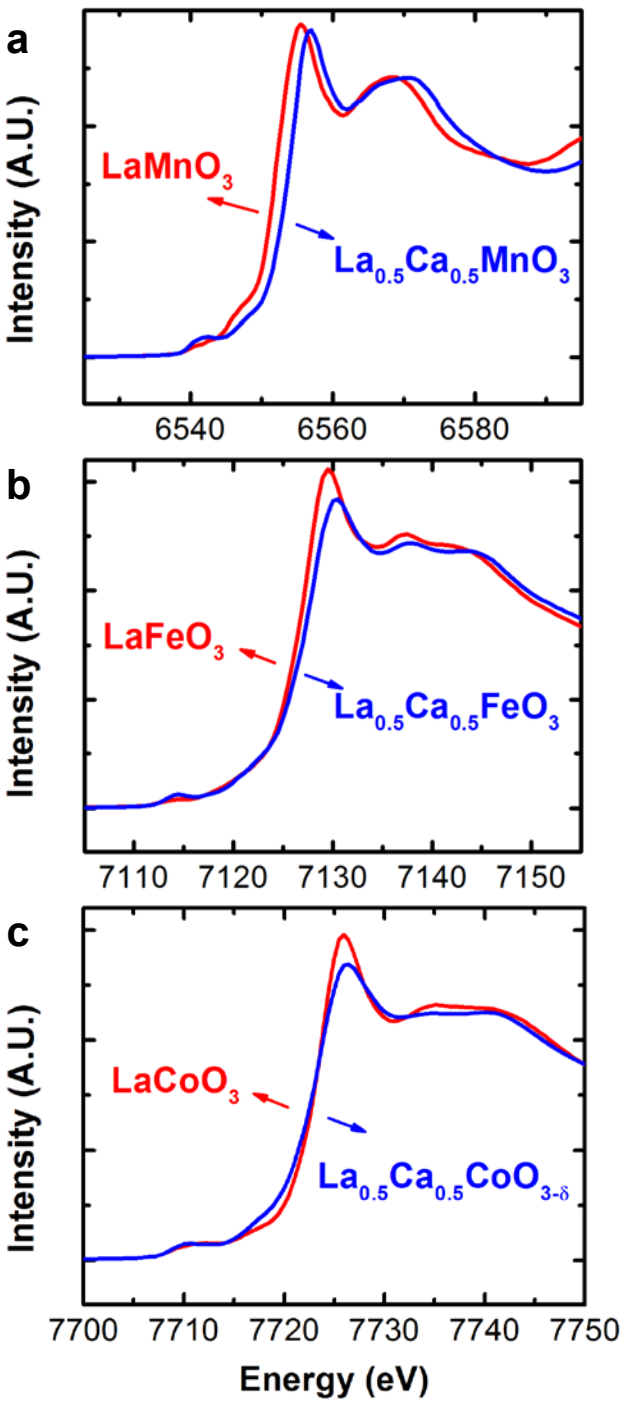

Figure S3. XANES of $LaBO_3$ perovskite oxides vs. Ca-containing $LaBO_3$ ($La_{0.5}Ca_{0.5}BO_3$). (a) B = Mn. The energy

position of the $La_{0.5}Ca_{0.5}MnO_3$ Mn K-edge is higher than that of $LaMnO_3$, which suggests that Mn in $La_{0.5}Ca_{0.5}MnO_3$, on average, has a higher oxidation state than $LaMnO_3$. (b) and (c) Similar analyses for B = Fe and Co respectively.

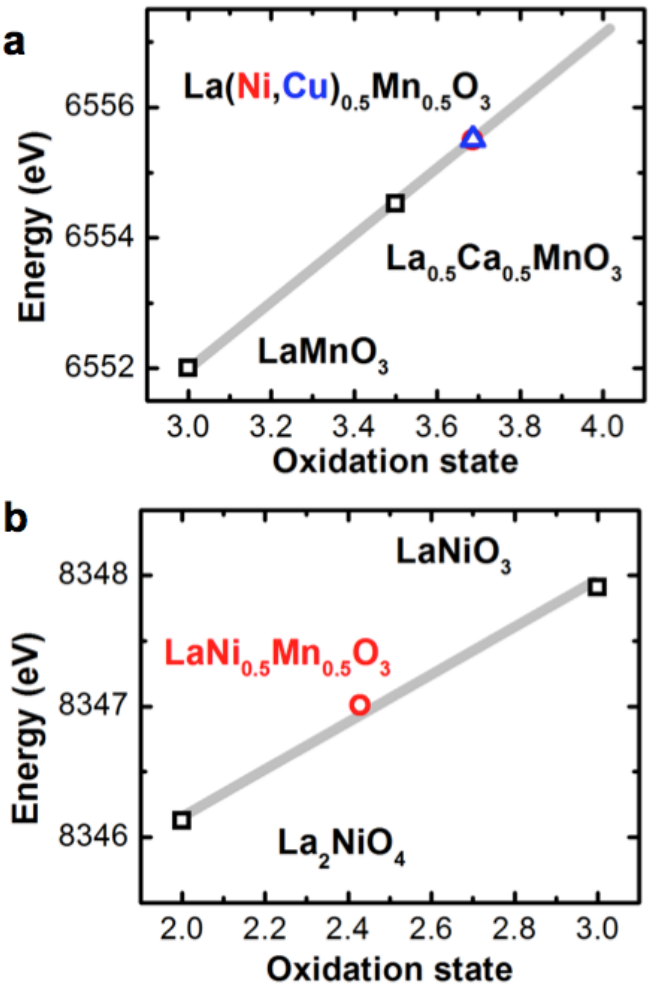

Figure S4. Determination of oxidation state of Mn in $LaNi_{0.5}Mn_{0.5}O_3$ and $LaCu_{0.5}Mn_{0.5}O_3$ using XAS E_0's relationship with the oxidation state. (a) Mn oxidation state for both mixed compounds (● for $LaNi_{0.5}Mn_{0.5}O_3$, ▲ for $LaCu_{0.5}Mn_{0.5}O_3$) is determined to be ≈3.7+. (b) Similar analysis as (a) for Ni in $LaNi_{0.5}Mn_{0.5}O_3$ (●). The oxidation state for Ni is determined to be ≈2.3+.

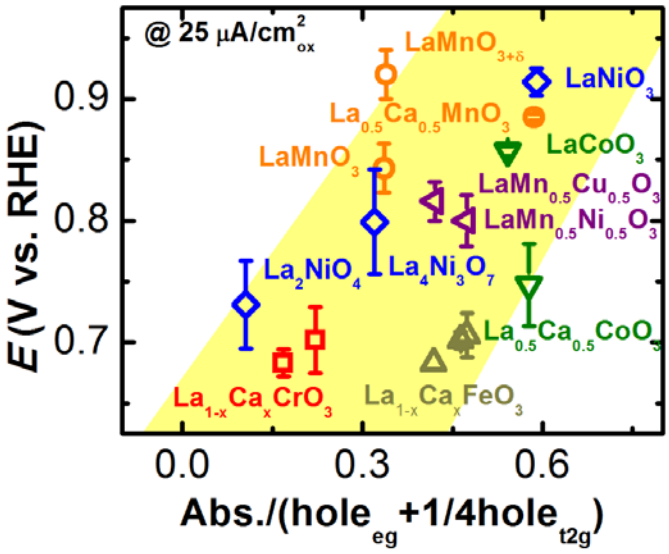

Figure S5. The ORR benchmark potentials as a function of the normalized absorbance. The weak dependence of the activity on the hybridization parameter is guided through a yellow band in the background. The data symbols vary with the type of B ions (■ for Cr, ● for Mn, ▲ for Fe, ▼ for Co, ◆ for Ni, and ◄ for mixed compounds), where x = 0 and 0.5 for Cr, and 0, 0.25, and 0.5 for Fe. Error bars represent standard deviations of at least three independent measurements.

References

1. Medarde, M. et al., Low-temperature spin-state transition in $LaCoO_3$ investigated using resonant x-ray absorption at the Co K edge. *Phys. Rev. B* **73,** 054424 (2006).
2. de Groot, F. M. F. et al., Oxygen 1s X-ray-absorption edges of transition-metal oxides. *Phys. Rev. B* **40,** 5715-5723 (1989).
3. Ravel, B. & Newville, M., ATHENA, ARTEMIS, HEPHAESTUS: data analysis for X-ray absorption spectroscopy using IFEFFIT. *J. Synchrot. Radiat.* **12,** 537-541 (2005).
4. Tyson, T. A. et al., Valence state of Mn in Ca-doped $LaMnO_3$ studied by high-resolution Mn K-beta emission spectroscopy. *Phys. Rev. B* **60,** 4665-4674 (1999).
5. Croft, M. et al., Systematic Mn *d*-configuration change in the $La_{1-x}Ca_xMnO_3$ system: A Mn K-edge XAS study. *Phys. Rev. B* **55,** 8726-8732 (1997).
6. Ritter, C. et al., Influence of oxygen content on the structural, magnetotransport, and magnetic properties of $LaMnO_{3+\delta}$. *Phys. Rev. B* **56,** 8902-8911 (1997).
7. Yan, J. Q., Zhou, J. S., & Goodenough, J. B., Ferromagnetism in $LaCoO_3$. *Phys. Rev. B* **70,** 014402 (2004).
8. Takeda, T., Watanabe, H., & Yamaguch.Y, Magnetic Structure of $SrCoO_{2.5}$. *J. Phys. Soc. Jpn.* **33,** 970-& (1972).
9. Arcon, I., Mirtic, B., & Kodre, A., Determination of valence states of chromium in calcium chromates by using X-ray absorption near-edge structure (XANES) spectroscopy. *J. Am. Ceram. Soc.* **81,** 222-224 (1998).
10. Russo, U. et al., Local interactions and electronic phenomena in substituted $LaFeO_3$ perovskites. *Solid State Ionics* **176,** 97-102 (2005).
11. Yan, J. Q., Zhou, J. S., & Goodenough, J. B., Bond-length fluctuations and the spin-state transition in $LCoO_3$ (L=La, Pr, and Nd). *Phys. Rev. B* **69,** 134409 (2004).
12. Medarde, M. L., Structural, magnetic and electronic properties of $RNiO_3$ perovskites (R equals rare earth). *J Phys-Condens Mat* **9,** 1679-1707 (1997).

13. Zhou, J. S. et al., Enhanced susceptibility in $LNiO_3$ perovskites (L = La, Pr, Nd, $Nd_{0.5}Sm_{0.5}$). *Phys. Rev. Lett.* **84,** 526-529 (2000).

14. Suntivich, J., Gasteiger, H. A., Yabuuchi, N., & Shao-horn, Y., Electrocatalytic measurement methodology of oxide catalysts using a thin-film rotating disk electrode. *J. Electrochem. Soc.* **157,** B1263-B1268 (2010).